INFLUENCE OF DETAILED DIFFUSION PROCESSES ON TURBULENT MIXING IN TEMPORAL COMPRESSIBLE SHEAR LAYERS WITH SPECIES AND TEMPERATURE GRADIENTS

Inga Mahle, Joern Sesterhenn, Rainer Friedrich
Fachgebiet Stroemungsmechanik,
Technische Universitaet Muenchen
Boltzmannstr. 15, 85748 Garching, Germany
mahle@flm.mw.tu-muenchen.de

Alexandre Ern
CERMICS, ENPC
6 et 8, av. Blaise Pascal, 77455 Marne la Vallée cedex 2, France
ern@cermics.enpc.fr

ABSTRACT

Besides a simplified treatment of chemistry, many existing turbulent combustion models also use simplified diffusion processes (Hilbert et al., 2004). Differential and thermal diffusion effects are only included in recent DNS of turbulent combustion, for example in de Charentenay and Ern (2002) and show mainly local influence on the flame structure. Since for non-premixed test cases exact modeling of the mixing process is a prerequisite of correct combustion predictions, the goal of our work is to further investigate the effects of detailed diffusion, modelled at different levels of precision, on turbulent mixing in the non-reacting case.

Motivated by this, DNS of temporally evolving, turbulent compressible shear layers with gradients of species and temperature have been performed.

The species are called active scalars because they influence the flow via the density due to their different molecular weights and via the transport coefficients like heat conductivity and diffusion coefficients.

Two different levels of approximation for the species diffusion fluxes and the heat flux are used and their effects are investigated. A quantity of special interest in this paper is the scalar dissipation rate as it is directly related to the reaction rate in combustion and therefore important for combustion modeling, for example in LES.

The first section of the paper describes the configurations and the initial parameters of the simulations. Then, the Navier-Stokes and species transport equations including detailed or simplified diffusion are presented. A self-similar state from which mean profiles and statistics are taken is defined in the following section. Next, mean profiles of diffusion flux and heat flux are analyzed. With the help of the diffusion flux, a mean Schmidt number is defined and its profile is evaluated which allows to assess the approximation of a spatially constant Schmidt number for each species. After this, the influence of the diffusion description on mean profiles, instantaneous fields and pdfs of the scalar dissipation rate or related quantities is investigated. Finally, conclusions are drawn.

SHEAR LAYER CONFIGURATION AND INITIAL PARAMETERS

Fig. 1 shows the configuration of the shear layer. All test cases are 3D with x and y denoting the streamwise and spanwise directions and z denoting the transverse direction of the planar shear layer. The upper stream (index 1) is pure oxygen while the lower stream (index 2) is a mixture of hydrogen and oxygen with mass fractions Y_α chosen in such a way that the ratio of the molecular weight for the mixture between this stream and the upper stream is 1:2. Greek indices denote the species.

In the first two test cases, denoted O_2-H_2-1-*dd* with detailed diffusion and O_2-H_2-1-*sd* with simplified diffusion, the temperature of the upper stream ($T_1 = 586.30\ K$) is two times the temperature of the lower stream ($T_2 = 293.15\ K$) in order to have equal density ($\rho_1 = \rho_2 = 0.66\ kg/m^3$). Simplified diffusion means the neglection of thermal and cross diffusion effects (see following section).

In the second series of test cases, denoted O_2-H_2-4-*dd* with detailed diffusion and O_2-H_2-4-*sd* with simplified diffusion, a mean density gradient is present: The temperature of the lower stream ($T_2 = 586.30\ K$) is two times the temperature of the upper stream ($T_1 = 293.15\ K$) which results in a density ratio of 4:1 ($\rho_1 = 1.32\ kg/m^3$, $\rho_2 = 0.33\ kg/m^3$).

These two series of test cases allow to compare the influences of detailed and simplified diffusion on quantities that are constitutive for mixing and combustion. The importance of these effects can be assessed depending on which stream is the hotter one, the stream with the lighter molecules or the other one.

The turbulent velocity and the nearly constant ($p_1 \approx p_2 \approx 10^5\ Pa$) pressure field of another shear layer are used for initialization. This shear layer with constant density was computed previously for a Reynolds number

$$Re_{\omega,b} = \frac{\Delta u \cdot \rho_{ref} \cdot \delta_{\omega,b}}{\mu_{ref}} = 4992 \qquad (1)$$

based on the momentary vorticity thickness $\delta_{\omega,b}$. Δu denotes the velocity difference. The reference density is $\rho_{ref} =$

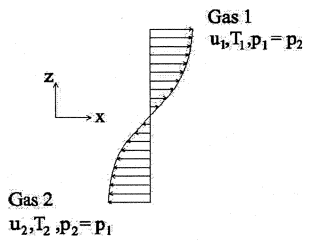

Figure 1: The schematic configuration of the shear layer

Table 1: Geometrical parameters for the simulations. The computational domain has the dimensions L_x, L_y and L_z with N_x, N_y and N_z grid points, respectively.

L_x/δ_{ref}	L_y/δ_{ref}	L_z/δ_{ref}	$Nx \times N_y \times N_z$
86.25	21.50	43.16	512 x 128 x 256

$(\rho_1 + \rho_2)/2$. The reference dynamic viscosity μ_{ref} is evaluated in the middle of the shear layer. The convective Mach number

$$Ma_c = \frac{\Delta u}{c_1 + c_2} \tag{2}$$

is 0.11 for the test cases O_2-H_2-1 and 0.10 for the test cases O_2-H_2-4, reflecting the low Mach number situation in combustion devices like combustion chambers. c_1 and c_2 are the sonic speeds of the streams. The temperature and the density are initialized by a hyperbolic-tangent profile and the species mass fractions are computed via the ideal gas law.

Grid and domain sizes are the same for all test cases and are given in table 1. The domain sizes are based on a reference length

$$\delta_{ref} = \delta_{\omega,b} \cdot \frac{Re_{\omega,0}}{Re_{\omega,b}} \tag{3}$$

computed with the initial Reynolds number $Re_{\omega,0} = 640$ of the shear layer computation from which the turbulent velocity field is taken. The domain sizes are comparable to those which Pantano and Sarkar (2002) have used for their DNS of a shear layer with a density ratio of 4. The grid-spacing of all test cases is constant in x- and y-directions. In the z-direction, approximately the inner third of the domain has a constant grid-spacing with $\Delta z_{min} = 0.126 \cdot \delta_{ref}$ while the stretching in the external parts is 3 %. The boundary conditions are periodic in x- and y-directions and nonreflective in z-direction.

NAVIER-STOKES AND SPECIES TRANSPORT EQUATIONS AND THEIR NUMERICAL INTEGRATION

The compressible Navier-Stokes and species transport equations are solved in a pressure-velocity-entropy-species formulation (Sesterhenn, 2001):

$$\begin{aligned}
\frac{\partial p}{\partial t} + u_i \frac{\partial p}{\partial x_i} &= -\rho c \frac{\partial u_i}{\partial x_i} + (\gamma - 1)\left(\tau_{ij}\frac{\partial u_i}{\partial x_j} - \frac{\partial q_i}{\partial x_i}\right) \\
&\quad + \sum_\alpha \left[(\gamma - 1)\, h_\alpha - \gamma \frac{\mathcal{R}T}{W_\alpha}\right] \frac{\partial}{\partial x_i}\left(\rho Y_\alpha V_{\alpha i}\right) \\
\frac{\partial u_i}{\partial t} + u_j \frac{\partial u_i}{\partial x_j} &= \frac{1}{\rho}\left(-\frac{\partial p}{\partial x_i} + \frac{\partial \tau_{ij}}{\partial x_j}\right) \\
\frac{\partial s}{\partial t} + u_i \frac{\partial s}{\partial x_i} &= \frac{1}{\rho T}\left(\tau_{ij}\frac{\partial u_i}{\partial x_j} - \frac{\partial q_i}{\partial x_i}\right) \\
&\quad + \frac{1}{\rho T}\sum_\alpha \left(h_\alpha - T s_\alpha\right) \frac{\partial}{\partial x_i}\left(\rho Y_\alpha V_{\alpha i}\right) \\
\frac{\partial Y_\alpha}{\partial t} + u_i \frac{\partial Y_\alpha}{\partial x_i} &= -\frac{1}{\rho}\frac{\partial}{\partial x_i}\left(\rho Y_\alpha V_{\alpha i}\right)
\end{aligned} \tag{4}$$

Pressure, velocity and entropy are denoted respectively by p, u_i and s. The density is ρ, the sonic speed c, the viscous stress tensor τ_{ij} and the universal gas constant $\mathcal{R} = 8.314\ J/(kg \cdot mol)$. W_α is the molecular weight of species α. Polynomial expressions (Gardiner, 1984) are used to compute the enthalpy h_α and entropy s_α of each species and the specific heats of the mixture to determine their ratio γ.

The species diffusion flux $Y_\alpha V_{\alpha i}$ with the diffusion velocity $V_{\alpha i}$ is evaluated as

$$Y_\alpha V_{\alpha i} = -\sum_\beta Y_\alpha D_{\alpha\beta} d_{\beta i} - Y_\alpha \theta_{\alpha i} \frac{\partial ln T}{\partial x_i} \tag{5}$$

with the diffusion vector

$$d_{\beta i} = \frac{\partial X_\beta}{\partial x_i} + \left(X_\beta - Y_\beta\right) \frac{\partial ln p}{\partial x_i} \tag{6}$$

where X_β is the mole fraction of species β. The transport coefficients, namely the flux diffusion matrix $D_{\alpha\beta}$ and the thermal diffusion vector $\theta_{\alpha i}$, are evaluated with the help of the program EGlib (Ern and Giovangigli, 1995) that is integrated into our code. It incorporates the local temperature, pressure and species' composition to compute the transport coefficients.

In addition, the heat flux

$$q_i = \sum_\alpha \rho h_\alpha Y_\alpha V_{\alpha i} - \lambda' \frac{\partial T}{\partial x_i} - p \sum_\alpha \theta_\alpha d_{\alpha i} \tag{7}$$

requires the partial thermal conductivity λ' which is also given by EGlib. This program offers the possibility to use different levels of approximation for the species diffusion fluxes and the heat flux. The most detailed description is given by eq.(5) and eq.(7). It takes into account the thermodiffusion effects given by the terms with θ_α as well as cross diffusion effects represented by $D_{\alpha\beta}$. In the simplified description, thermodiffusion is neglected and the Hirschfelder-Curtiss approximation (Hirschfelder et al., 1954) for the species diffusion coefficients in the mixture is used neglecting cross diffusion effects. A correction velocity is considered to ensure mass conservation. Radiation effects are neglected in both descriptions of the heat flux.

The integration of equations (4) is performed using sixth order compact central schemes for the spatial derivatives and a third order low-storage Runge-Kutta scheme for time integration. The primitive variables are filtered all the 20 time steps to prevent spurious accumulation of energy in the highest wavenumbers using a sixth-order compact filter.

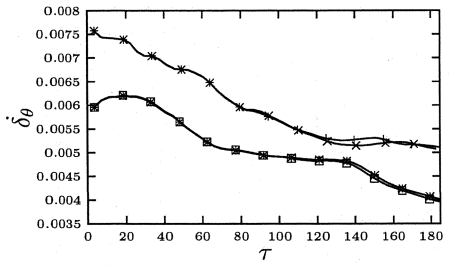

Figure 2: Dimensionless growth rate of the momentum thickness, ×: O_2-H_2-1-*sd*, +: O_2-H_2-1-*dd*, □: O_2-H_2-4-*sd*, ∗: O_2-H_2-4-*dd*

The code is parallelized and the simulations were performed on up to 128 processors of the supercomputer Hitachi SR8000-F1 of the Leibniz-Rechenzentrum in Munich (Germany). Each computation required up to 24500 CPUh.

THE SELF-SIMILAR STATE

All computations are performed over times that are long enough to reach a self-similar state (Pantano and Sarkar, 2002). In fact, after an initial transient, an approximately constant dimensionless growth rate

$$\dot{\delta}_\theta = -\frac{2}{\rho_0 \Delta u^3} \int_{-\infty}^{\infty} \overline{\rho u'' w''} \frac{\partial \tilde{u}}{\partial z} dz \tag{8}$$

for the momentum thickness is established which depends on the density gradient (fig. 2). Quantities with an overbar, like $\overline{\rho}$, are Reynolds averaged quantities, quantities with a tilde, like $\tilde{u}$, are Favre averaged quantities. Primes and double primes indicate the respective fluctuations. The non-dimensional time is

$$\tau = \frac{t \cdot \Delta u}{\delta_{ref}} \tag{9}$$

with the physical time t. The differences in growth rate between the respective simulations with detailed and with simplified diffusion are small. In qualitative agreement with Pantano and Sarkar (2002), we notice a drop in the growth rate for the test cases with density gradient.

The fact that the growth rate remains constant over a certain period of time allows the definition of an intermediate self-similar state at which enough vortex structures are present in the domain to neglect the influence of the finite domain size. Figure 11 shows the instantaneous hydrogen mass fraction for such a state at $\tau = 128$.

Pantano and Sarkar (2002) suggest the non-dimensionalization by the variables δ_θ, ρ_0 and Δu. This is done in fig. 3 for the scalar variance

$$\widetilde{Y''^2} = \frac{\overline{\rho Y'' Y''}}{\overline{\rho}} \tag{10}$$

of O_2-H_2-4-*sd*. Here and in the following denote $Y = Y_{H_2}$ and $V_i = V_{H_2,i}$ etc. The relaxation to a self-similar state is visible. The profiles are shifted towards the side of the lower density because the so-called dividing streamline has moved there, which can be explained by the mean-momentum conservation (Pantano, 2000).

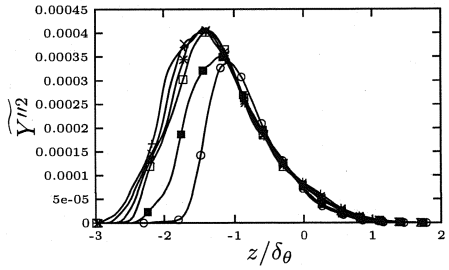

Figure 3: Instantaneous profiles of scalar variance, O_2-H_2-4-*sd*, ○: $\tau = 88$, ■: $\tau = 125$, □: $\tau = 154$, ∗: $\tau = 161$, ×: $\tau = 168$, +: $\tau = 176$

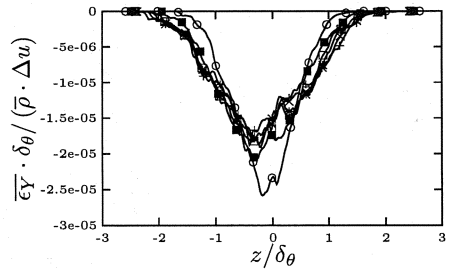

Figure 4: Instantaneous profiles of scalar dissipation, O_2-H_2-1-*sd*, ○: $\tau = 41$, ■: $\tau = 83$, □: $\tau = 114$, ∗: $\tau = 121$, ×: $\tau = 129$, +: $\tau = 137$

Table 2: Dimensionless time and Reynolds number at the beginning (index: B) and end (index: E) of the self-similar state

	O_2-H_2-1-*sd* (*dd*)	O_2-H_2-4-*sd* (*dd*)
τ_B	114	161
τ_E	156	176
$Re_{\omega,B}$	11181 (10766)	13680 (14140)
$Re_{\omega,E}$	14058 (12973)	14793 (15525)

A collapse of the profiles for the self-similar state is observed as well for the mean scalar dissipation rate

$$\overline{\epsilon_Y} = -\overline{\rho Y V_i \frac{\partial Y''}{\partial x_i}} \tag{11}$$

which appears in the transport equation of the scalar variance (for example O_2-H_2-1-*sd* in fig. 4) .

The beginning and end of the so defined self-similar states are given in table 2 along with the Reynolds numbers

$$Re_\omega = Re_{\omega,0} \cdot \frac{\delta_\omega}{\delta_{ref}} \tag{12}$$

at these times. Due to the fact that the initial turbulent velocity field originates from a shear layer with constant density, it takes longer for the shear layers with density gradient to reach the self-similar state.

All mean profiles in this paper are averaged, both in time over the self-similar state and in space over the two homogeneous directions. The samples from which pdfs are built are taken from self-similar states.

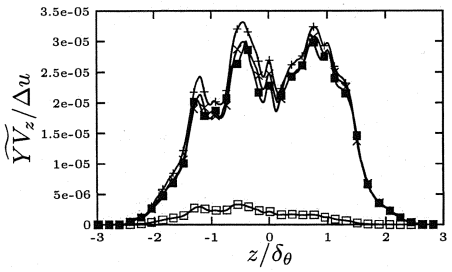

Figure 5: Components of the mean hydrogen diffusion flux, O_2-H_2-1, +: total (*dd*), ×: diffusive part (*dd*), □: thermodiffusive part (*dd*), ■: total (*sd*)

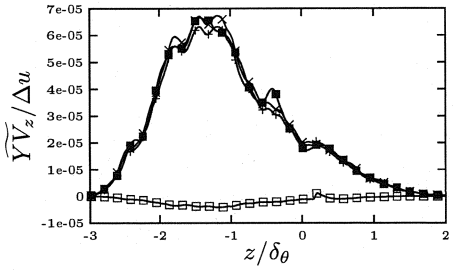

Figure 6: Components of the mean hydrogen diffusion flux, O_2-H_2-4, +: total (*dd*), ×: diffusive part (*dd*), □: thermodiffusive part (*dd*), ■: total (*sd*)

COMPONENTS OF DIFFUSION FLUX AND HEAT FLUX

In the detailed description of the diffusion, the diffusion flux has two parts: The diffusive part which is the first term on the right hand side (RHS) of eq.(5) and the thermodiffusive part (Soret effect) which is the second term and gives the species diffusion induced by temperature gradients. In the simplified description, the Soret effect is neglected. In the heat flux, eq.(7), the diffusive part (third term on RHS), namely the Dufour effect, is likewise only retained in the detailed description of the diffusion. The conductive part (second term) and the diffusive part (first term) are present in both descriptions, however, the last one with the Hirschfelder-Curtiss approximation in the simplified description.

Fig. 5 shows the different parts of the hydrogen diffusion flux for O_2-H_2-1-*dd*. Due to mass conservation, the oxygen diffusion flux has the same amount, but opposite sign. The Soret effect contributes up to 10 % in the interior of the shear layer. It is stronger on the hydrogen side and enhances the diffusion of the light hydrogen molecules towards the hot oxygen stream. In O_2-H_2-1-*dd* where the stream with the lighter molecules is also the hotter one, the direction of the thermodiffusive heat flux changes and its importance (up to 7 %) decreases (fig. 6).

In general, the Dufour effect in the heat flux (fig. 7 and fig. 8) is smaller than the Soret effect. But in O_2-H_2-1, as the diffusive part and the conductive parts have opposite signs and not too different sizes, the influence of the Dufour effect on their small sum can be considerable (for example at $z/\delta_\theta \approx 1.5$). However, high temperature gradients, like they are expected in combustion, enhance the negative conductive part which diminishes the importance of the diffusive and thermodiffusive parts even though the latter one is expected to increase somewhat, too. The positive sign of the diffusive heat flux is due to the fact that at the same temperature the specific entropy of hydrogen, whose diffusion velocity is positive (fig. 5), is higher than that of oxygen. In the mean heat flux of O_2-H_2-4 (fig. 8), the conductive and diffusive parts are both mostly positive. Therefore, the influence of the thermodiffusion decreases. The change in sign of the conductive heat flux around $z/\delta_\theta = 0.2$ is due to an unsteadiness in the slope of the mean temperature profile.

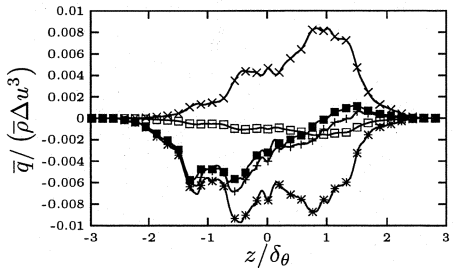

Figure 7: Components of the mean heat flux, O_2-H_2-1, +: total, ×: diffusive part (*dd*), ∗: conductive part (*dd*), □: thermodiffusive part (*dd*), ■: total (*sd*)

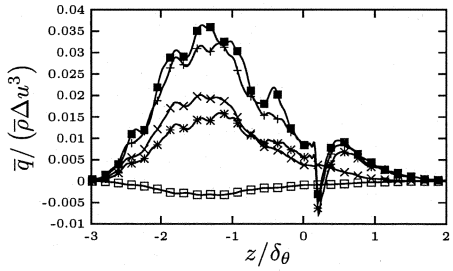

Figure 8: Components of the mean heat flux, O_2-H_2-4, +: total, ×: diffusive part (*dd*), ∗: conductive part (*dd*), □: thermodiffusive part (*dd*), ■: total (*sd*)

THE SCHMIDT NUMBER

A common simplification in combustion modeling is to assume a spatially constant Schmidt number

$$Sc = \frac{\mu}{\rho D} \tag{13}$$

for each species with D denoting the diffusion coefficient of the respective species and μ the dynamic viscosity. The diffusion flux according to Fick's law is then given by

$$\begin{aligned} YV_i &= -D\frac{\partial Y}{\partial x_i} \\ &= -\frac{\mu}{\rho Sc}\frac{\partial Y}{\partial x_i} \end{aligned} \tag{14}$$

If we insert our detailed or simplified diffusion flux YV_i, we can compute a mean Schmidt number

$$\overline{Sc} = -\overline{\frac{\mu}{\rho YV_i}\frac{\partial Y}{\partial x_i}} \tag{15}$$

Having only two species whose diffusion fluxes and mass fraction gradients have opposite sign but the same amount, the two species have necessarily the same Schmidt number in order to guarantee mass conservation. Fig. 9 shows this mean

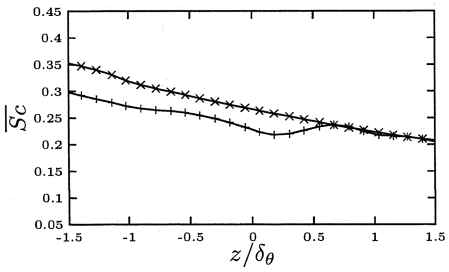

Figure 9: Schmidt number according to eq.(15), averaged for the self-similar state, ×: O_2-H_2-1-*sd*, +: O_2-H_2-1-*dd*

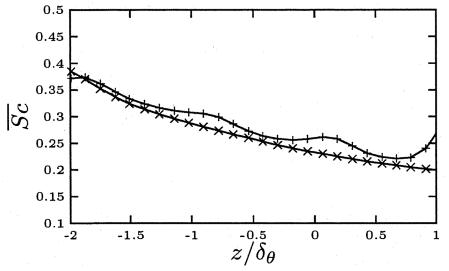

Figure 10: Schmidt number according to eq.(15), averaged for the self-similar state, ×: O_2-H_2-4-*sd*, +: O_2-H_2-4-*dd*

Schmidt number for O_2-H_2-1 in the centre of the shear layer. For the simplified diffusion, it varies between 0.21 and 0.35. The detailed diffusion decreases the Schmidt number by up to 14 % on the hydrogen side but has little influence on the oxygen side. The effect of the detailed diffusion on the Schmidt number of O_2-H_2-4 is different: It increases in the whole centre of the shear layer (fig. 10). As shown in the previous section, the fact that the hotter stream contains the lighter molecules, decreases the influence of the thermodiffusion. Therefore, the changes in Schmidt number are not as pronounced as in O_2-H_2-1. However, the Schmidt number is not constant in transverse direction either, which rules out a realistic combustion simulation with such an assumption.

INFLUENCE OF DIFFUSION ON INSTANTANEOUS FIELDS AND MEAN PROFILES

Figure 11 shows the instantaneous hydrogen mass fraction field for a self-similar state of O_2-H_2-1. One can see that there are local differences in the isolines. However, the large structures are the same in both test cases and there are no differences visible in the corresponding mean profile in all test cases (not shown). The influence on the mean profiles of other quantities like the scalar dissipation rate (for example for O_2-H_2-4 in fig. 12) is small as well.

PDFS OF SCALAR GRADIENTS AND SCALAR DISSIPATION RATE

The influence of the diffusion description on the mean scalar dissipation rate was found to be small. However, in combustion, the instantaneous scalar dissipation rate plays an important role as its local maxima correspond to regions of intense reaction. In addition, very large deviations from the mean scalar dissipation rate can cause local flame extinction.

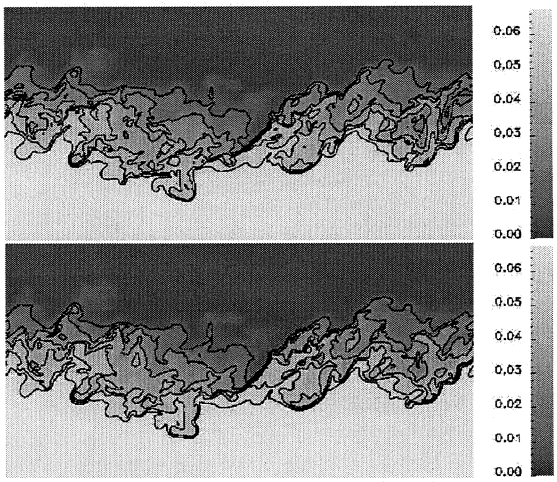

Figure 11: Instantaneous mass fraction field of H_2, top: O_2-H_2-1-*sd*, bottom: O_2-H_2-1-*dd*, $\tau = 128$, x-z-plane in the middle of the domain, isolines with increment 0.01 shown

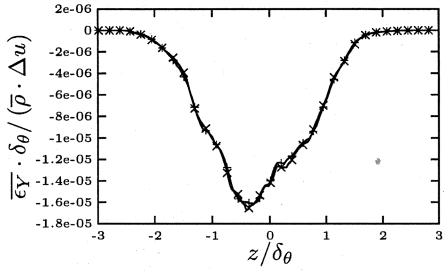

Figure 12: Mean scalar dissipation rate, ×: O_2-H_2-1-*sd*, +: O_2-H_2-1-*dd*

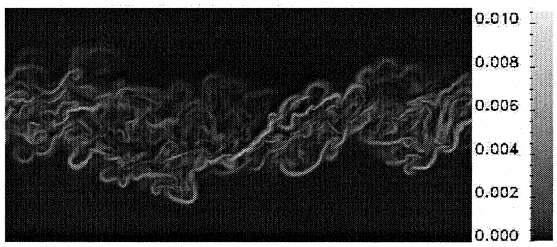

Figure 13: Instantaneous magnitude of the scalar gradient $\frac{\partial Y_{H_2}}{\partial x_i}$ normalized with $\delta_{\omega,b}$, O_2-H_2-1-*sd*, $\tau = 128$, x-z-plane in the middle of the domain

Scalar gradients and scalar dissipation rate share many features as the latter is computed from the gradients of the Favre scalar fluctuations (eq.(11)). Fig. 13 shows the instantaneous magnitude of the hydrogen gradient. The field is very intermittent with large values that do occur but with a very low frequency.

The high intermittency can also be seen in the pdfs of the scalar gradients. The pdfs of the scalar derivatives in transverse direction (samples taken from the centre of the mixing layer, from six planes around $\widetilde{Y}/\widetilde{Y}_{max} = 0.5$) are shown in fig. 14. The differences between the respective test cases with simplified and detailed diffusion are predominantely found in the

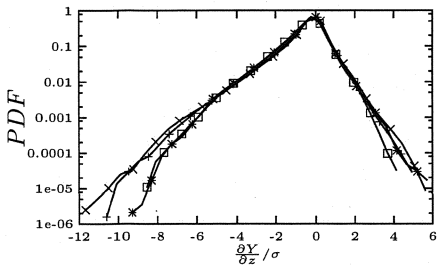

Figure 14: Pdf of the transverse scalar derivative normalized by its variance σ, centre of the shear layer, $\times$: O_2-H_2-1-*sd*, $+$: O_2-H_2-1-*dd*, $\Box$: O_2-H_2-4-*sd*, $*$: O_2-H_2-4-*dd*

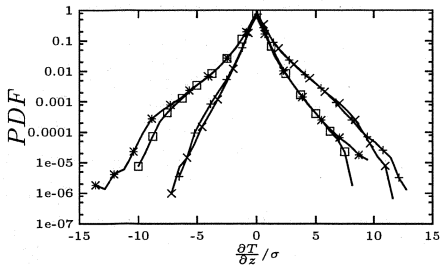

Figure 15: Pdf of the transverse temperature derivative normalized by its variance σ, centre of the shear layer, $\times$: O_2-H_2-1-*sd*, $+$: O_2-H_2-1-*dd*, $\Box$: O_2-H_2-4-*sd*, $*$: O_2-H_2-4-*dd*

Table 3: Maximal value of the scalar dissipation rate

	O_2-H_2-1-*sd* (*dd*)	O_2-H_2-4-*sd* (*dd*)
$(\epsilon_Y/\overline{\epsilon_Y})_{max}$	63.2 (52.1)	48.3 (46.9)

tails of the pdfs. The skewness of the pdfs can be related to sharp scalar fronts (Holzer and Siggia, 1994), (Pumir, 1994). These ramp-cliff events result from the transit of fluid lumps along the imposed gradient from the low-scalar region towards the high-scalar region and vice versa (Gonzalez, 2000).

The fact that the sign of the skewness is related to the mean gradient can be seen from fig. 15 which shows the pdfs of the transverse temperature derivative: In O_2-H_2-1 where the mean temperature gradient is positive, the skewness is positive. In O_2-H_2-4 where the direction of the mean temperature gradient is opposite, the sign of the skewness also changes.

The high intermittency of the scalar gradients leads to a high intermittency of the scalar dissipation which is confirmed by its pdf, for example in fig. 16 where rare large values appear. The description of the diffusion has an influence on the largest appearing value in both series of test cases: The maxima is increased by using the simplified diffusion, even by 21 % in O_2-H_2-1-*sd*. The exact values are given in table 3.

CONCLUSIONS

Summing up, the influence of the diffusion description in DNS of turbulent shear layers with species and temperature

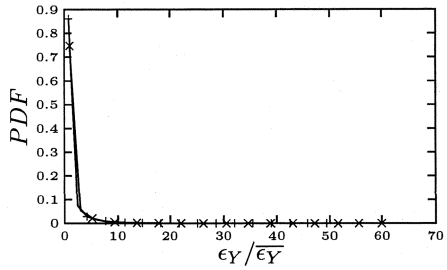

Figure 16: Pdf of the scalar dissipation, centre of the shear layer, $\times$: O_2-H_2-1-*sd*, $+$: O_2-H_2-1-*dd*

gradients is predominantly instantaneous and local. The turbulent fluctuations appear to filter out to a great extent these effects when considering mean quantities which was also observed by de Charentenay and Ern (2002) for premixed flames. Nevertheless, they are still visible, for example when regarding the mean Schmidt number. Their importance increases when light molecules like H_2 are next to hot zones. Local changes by the diffusion, for example of the scalar dissipation rate, are found to be quite strong. Increases of the instantaneous scalar dissipation rate can lead to significant changes in flame behaviour like local extinction. Therefore, it seems to be important to retain as far as possible detailed diffusion effects in combustion simulations.

REFERENCES

de Charentenay, J., and Ern, A., 2002, "Multicomponent transport impact on premixed turbulent H2/O2 flames", *Combustion Theory and Modelling*, Vol. 6, pp. 463-478.

Ern, A., and Giovangigli, V., 1995, "Fast and accurate multicomponent transport property evaluation", *Journal of Computational Physics*, Vol. 120, pp. 105-116.

Gardiner, W., 1984, *Combustion Chemistry*, Springer, New York.

Gonzalez, M., 2000, "Study of the anisotropy of a passive scalar field at the level of dissipation", *Physics of Fluids*, Vol. 12, pp. 2302-2310.

Hilbert, R., Tap, F., El-Rabii, H., and Thévenin, D., 2004, "Impact of detailed chemistry and transport models on turbulent combustion simulations", *Progress in Energy and Combustion Science*, Vol. 30, pp. 61-117.

Hirschfelder, J.O., Curtiss, C.F., and Bird, R.B., 1954, *Molecular theoury of gases and liquids*, Wiley, New York.

Holzer, M., and Siggia, E. D., 1994, "Turbulent mixing of a passive scalar", *Physics of Fluids*, Vol. 6, pp. 1820-1837.

Pantano, C., 2000, "Compressibility Effects in Turbulent Nonpremixed Reacting Shear Flows", Ph.D. Thesis, University of California, San Diego.

Pantano, C., and Sarkar, S., 2002, "Mixing of a conserved scalar in a turbulent reacting shear layer", *Journal of Fluid Mechanics*, Vol. 451, pp. 329-371.

Pumir, A., 1994, "A numerical study of the mixing of a passive scalar in three dimensions in the presence of a mean gradient", *Physics of Fluids*, Vol. 6, pp. 2118-2132.

Sesterhenn, J., 2001, "A characteristic-type formulation of the Navier-Stokes equations for high order upwind schemes", *Computers & Fluids*, Vol. 30, pp. 37-67.